Simulation of a Single Rotor and a Quadrotor Hovering in Full and Partial Ground Effect

Denis-Gabriel Caprace*, Patricia Ventura Diaz†, Seokkwan Yoon‡
NASA Ames Research Center
Moffett Field, CA, USA

With the development of urban air mobility, the safety of multirotor vehicle operations in proximity to vertiports must be assessed. This paper examines high-fidelity blade-resolved OVERFLOW simulations and medium-fidelity vortex particle–mesh simulations that capture the aerodynamics of a rotorcraft in full and partial ground effect. Results obtained with each CFD method are compared to verify the consistency of the models introduced in the latter, which include an immersed lifting line for the blade aerodynamics and various boundary conditions to account for solid surfaces such as ground and walls. Satisfactory agreement is obtained for the blade loads and rotorwash velocity profiles in the case of a single rotor, except for small discrepancies at the blade tip. Finally, a quadrotor air taxi is simulated to quantify the load imbalance when the vehicle hovers above a rooftop edge. The combined use of high- and medium-fidelity methods is envisioned to accelerate the workflow when a large number of configurations need to be tested.

I. Nomenclature

a	=	speed of sound $[\mathrm{m\,s^{-1}}]$
c	=	local chord length [m]
$c_n = \frac{f_n}{\frac{1}{2}\rho\|\|\mathbf{u}\|\|^2 c}$	=	sectional normal force coefficient $[-]$
D	=	rotor diameter [m]
H	=	rotor height above the ground [m]
h	=	grid spacing [m]
$\mathscr{M}$	=	rotor or vehicle moment [N m]
$M = \frac{\|\|\mathbf{u}\|\|}{a}$	=	Mach number
R	=	rotor radius [m]
$\mathscr{T}$	=	rotor or vehicle thrust [N]
T_{rev}	=	rotor revolution period [s]
t_{end}	=	physical time reached at the end of a simulation [s]
U_{tip}	=	blade tip velocity $[\mathrm{ms^{-1}}]$
$u_{x,y,z}$	=	velocity components $[\mathrm{m\,s^{-1}}]$
$V_H = \sqrt{\frac{\mathscr{T}}{2\rho(\pi R^2)}}$	=	reference induced velocity in hover $[\mathrm{m\,s^{-1}}]$
Δt	=	physical time step [s]
ρ	=	air density $[\mathrm{kg\,s^{-3}}]$
ψ	=	blade azimuth angle
$\omega_{x,y,z}$	=	vorticity components $[\mathrm{s^{-1}}]$

II. Introduction

The airflow induced by a vertical take-off and landing aircraft raises safety concerns when considering urban air mobility (UAM) operations close to the ground. The so-called rotorwash induced by a rotorcraft is generally

*Oak Ridge Associated Universities, NASA Postdoctoral Program fellow, AIAA member. Corresponding author: denis-gabriel.caprace@nasa.gov
†Science and Technology Corporation, AIAA member.
‡NASA Advanced Supercomputing Division.

unsteady and complex. Complexity increases in proximity to the ground because rotor wakes interact with the ground surface and nearby objects and structures. Additionally, mutual interactions between the rotorcraft wake and the airflow around these objects and structures may cause sudden changes in the aerodynamic loads of the blades. As a result, the performance of the rotor in ground effect (IGE) can be dramatically lowered. This increases the workload of the pilot, degrades the handling qualities of the vehicle, and increases noise levels [1]. Finally, in confined spaces, part of the flow may recirculate through the rotor, a condition that can lead to a vortex ring state [2]. These concerns have motivated a large number of studies on conventional helicopter operations close to the ground. However, few of them have focused on UAM applications.

Fig. 1 Illustration of a UAM vehicle in ground effect.

Fig. 2 NASA's quadrotor urban air taxi [3].

Over the past decades, the ground effect of a rotorcraft hovering over a flat surface has been the subject of numerous experimental studies. Preston et al. [4] have obtained full-scale rotorwash measurements for rotorcraft with various rotor arrangements (single rotor, tandem rotor, and tilt-rotor). Wind tunnel experiments have also been conducted. For example, Lee et al. [5] studied how rotor tip vortices interact with the flat ground. Tanner et al. [6] examined the rotorwash of a conventional helicopter configuration. Ramasamy and Yamauchi [7] compared isolated and tandem rotors to highlight the effect of the rotor arrangement on the measured velocity profiles. Dekker et al. [8] studied the flow patterns in the vicinity of side-by-side rotors in ground effect. The flow unsteadiness resulting from the interaction between the rotor wake and the ground has been the subject of dedicated studies as well [9].

Besides the simple flat-ground configuration, more complex geometries have been considered recently. At full scale, Silva et al. [10] studied the rotorwash of multiple helicopters and a tilt-rotor over an elevated platform and in confined space. At model scale, the GARTEUR action group [1] conducted multiple experiments to characterize the flow field and the performance of a hovering rotor in proximity to a cubic object. Pickles et al. [11] performed similar investigations. Experiments on helicopters have also been carried out in shipboard environments that present challenges similar to UAM operations (see, e.g., [12]).

In addition to these experimental efforts, numerical simulation has been used extensively for rotorcraft applications. For example, Hwang and Kwon [13] computed the flow past a S-76 rotor in and out of ground effect using blade-resolved high-fidelity overset CFD with unstructured grids. Numerous CFD simulations were also performed by the GARTEUR group [1]. Even so, the potential of CFD for IGE investigations has not yet been fully exploited [14]. In fact, the high computational cost associated with high-fidelity simulations of hovering rotorcraft near the ground often makes extensive aeromechanics and rotorwash studies impractical [15]. To alleviate the cost, some level of modeling can be introduced. Chirico et al. [16] considered a rotor hovering above a cubic object and compared flow predictions made by numerical simulations using blade-resolved and actuator disk approaches. Merabet and Laurendeau [17] simulated a hovering rotor in a confined space using an actuator line model for the blades. Another popular technique to simulate rotorcraft relies on vortex methods. Such methods are more computationally affordable than high-fidelity blade-resolved CFD and have shown promising results. For example, Zhao and He [18] predicted rotorwash over a flat ground quite accurately. Similar techniques were used to simulate the interaction between a single [19] or a tandem rotor [20] and a cubic obstacle.

Although a lot of literature exists on these topics, few studies have approached them with a UAM perspective. UAM operations present unique challenges. The fact that UAM vehicles often feature multirotor configurations is a departure from the majority of the existing literature. Consider an elevated vertiport located on a rooftop as illustrated in Fig. 1. A vehicle approaching the building from the side may experience an asymmetry when some rotors operate in ground effect and others operate out of ground effect [21]. This situation is termed *partial ground effect* in the remainder of this work. Likewise, an asymmetry can arise if flow recirculation occurs only on some rotors due to further interactions with the environment. This partial ground effect has the potential to decrease vehicle controllability or to create an upset situation, and thus calls for dedicated studies. Given the large diversity in both vehicle geometries and vertiport

configurations, there is a need for efficient computational tools to quickly assess the effect of aerodynamic interactions for a large number of vehicle-vertiport combinations.

This paper continues the effort started in [22] and aims to further highlight the potential of numerical simulation and modeling to respond to this challenge. In particular, the paper showcases how high-fidelity blade-resolved delayed detached eddy simulation (DDES) can be used to verify the results of medium-fidelity vortex simulation. The latter enables the study of aerodynamic interactions for a fraction of the high-fidelity computational cost. We illustrate this workflow using the case of a single rotor in full ground effect (IGE) above a flat ground and in partial ground effect (IPGE) above a rooftop edge. We evaluated different medium-fidelity models to account for the presence of solid surfaces such as the ground or building walls with a focus on the rotor performance and on the rotorwash velocity profile along the ground and wall. Finally, we present a preliminary study of partial ground effect on the NASA's quadrotor urban air taxi [3] (shown in Fig. 2). The quadrotor configuration in full and partial ground effect has received little attention in the literature compared to single or tandem rotor configurations.

III. Methods

A. High-fidelity solver

1. OVERFLOW

In the absence of experimental data on the geometry at hand, high-fidelity simulations are used as a reference in this study. They are performed with OVERFLOW [23]. OVERFLOW is a finite-difference, structured overset grid method that solves the unsteady Reynolds-averaged Navier-Stokes (RANS) equations for compressible flow in strong conservation form,

$$\frac{\partial \mathbf{q}}{\partial t} + \frac{\partial \left(\mathbf{F} - \mathbf{F}_v\right)}{\partial x} + \frac{\partial \left(\mathbf{G} - \mathbf{G}_v\right)}{\partial y} + \frac{\partial \left(\mathbf{H} - \mathbf{H}_v\right)}{\partial z} = \mathbf{0}, \tag{1}$$

with $\mathbf{q} = [\rho, \rho u_x, \rho u_y, \rho u_z, e]^\intercal$ the vector of conserved variables, $\mathbf{F}$, $\mathbf{G}$, $\mathbf{H}$ the inviscid flux vectors in the three directions, and $\mathbf{F}_v$, $\mathbf{G}_v$, $\mathbf{H}_v$ the viscous flux vectors. In the present study, time marching implements the second-order backward difference formula with dual time-stepping, and an implicit formulation of the subiterations.

The simulation settings used in this work follow the established best-practice guidelines for rotorcraft computations [24, 25]. In particular, the accurate computation of the figure of merit (FoM) requires the use of high-order schemes, a grid spacing of at most 10% of the tip chord in the near-wake region, and a time step no longer than the time needed for the rotor to rotate by 0.25°. In this work, spatial discretization utilizes the fourth-order accurate central difference scheme with matrix dissipation [26]. Time integration is performed using the second-order backward difference formula with dual time-stepping. At each iteration, we use up to 50 dual-time sub-iterations for a 2.5 to 3.0 orders of magnitude drop in the L2 norm of the flow residuals. Furthermore, the DDES capability of the code is employed, which combines the Spalart-Allmaras turbulence model close to the walls with a large eddy simulation (LES) formulation away from the wall. The numerical approach was previously validated for various rotor flows OGE [27, 28] and subsequently provided new insights into the aerodynamics of UAM vehicles [29, 30].

2. Grid assembly

NASA's Chimera Grid Tools (CGT) overset grid generation software is used to generate the overset grids of the rotors [31]. Body-fitted curvilinear near-body (NB) grids are generated using CGT. In practice, the same rotor grids as in [30] are used for the present study (Fig. 3). Additional NB grids are manually created near the surface of the flat ground and the building edge, following a procedure detailed in Section IV.B. The remainder of the domain consists of off-body (OB) grids. Cartesian OB grids with progressive coarsening can be generated automatically to fill the domain prior to grid assembly using the domain connectivity framework in OVERFLOW-D mode. This feature is used for the flat ground simulations. Alternatively, they can be generated manually, as is done for the rooftop edge in this work. For more details on the grid generation and assembly process, we again refer the reader to our previous publications [29, 30].

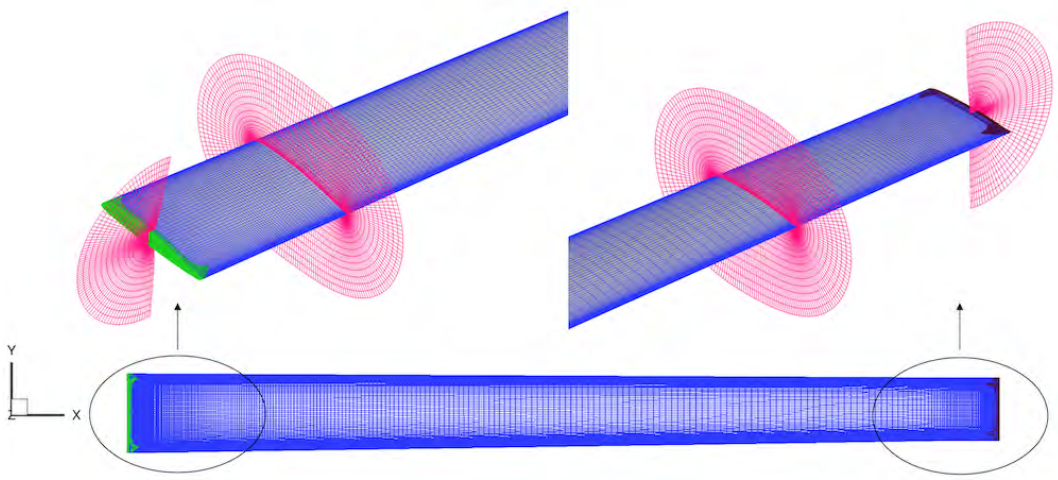

Fig. 3 Overset grids of one blade of the rotor. Cap grids are used for the root (green) and tip (brown), and an O-grid is used for the blade (blue). Slices of the volume grids are shown in magenta. The surface mesh uses 200 grid points spanwise and 286 chordwise. Refinement is used near the leading edge, trailing edge, blade tip, and blade root. The frame shown is local to the blade. Reproduced from [30].

B. Medium-fidelity solver

1. Vortex particle–mesh method

The vortex particle–mesh (VPM) method solves the Navier-Stokes equations for incompressible flow in their vorticity-velocity formulation,

$$\nabla \cdot \mathbf{u} = 0\,, \tag{2}$$

$$\frac{D\boldsymbol{\omega}}{Dt} = (\nabla \mathbf{u}) \cdot \boldsymbol{\omega} + \nu \nabla^2 \boldsymbol{\omega} + \nabla \cdot \mathbf{T}^M\,, \tag{3}$$

where $\mathbf{u}$ is the velocity, $\boldsymbol{\omega} = \nabla \times \mathbf{u}$ is the vorticity, $\frac{D}{Dt}$ denotes the Lagrangian derivative, ν is the kinematic viscosity, and $\mathbf{T}^M$ refers to the contribution of a sub-grid scale (SGS) model. The hybrid character of the VPM method comes from the combined use of a Lagrangian and a Eulerian discretization. On the one hand, vortex particles are employed to solve flow advection. The time integration here employs a third-order Runge-Kutta scheme. On the other hand, stretching and diffusion are solved on a background Cartesian grid through the use of fourth-order finite differences. The velocity field is computed by solving a Poisson equation,

$$\nabla^2 \mathbf{u} = -\nabla \times \boldsymbol{\omega}\,. \tag{4}$$

The Poisson solver [32, 33] takes advantage of the uniform grid resolution and operates in Fourier space, benefiting from an efficient 3D fast Fourier transform algorithm. As the particles move over time, high-order interpolation schemes are employed to exchange information between the particles and the grid. The SGS model used in this work is the regularized variational multiscale model [34]. It takes the same form as an eddy viscosity model but formulated for the vorticity,

$$\mathbf{T}^M = \nu_{\text{SGS}} \mathbf{Q}^{\mathbf{s}}\,, \tag{5}$$

where $\mathbf{Q} = \nabla \boldsymbol{\omega}^s - (\nabla \boldsymbol{\omega}^s)^\intercal$. $\boldsymbol{\omega}^s$ is the resolved high-wavenumber content of the vorticity field. It is obtained using a recursive filtering operation that also takes advantage of the mesh. The model was calibrated by Cocle et al. [35] and enables LES. The resulting method is known to have low dissipation and dispersion errors [36, 37], while being computationally efficient on massively parallel architectures [38]. Another advantage of this hybrid framework is that the constraint on the time step is usually less stringent than the classical Courant-Friedrichs-Lewy (CFL) condition in Eulerian solvers [39]. The present implementation uses adaptive time-stepping to maintain a Lagrangian CFL (LCFL) number below a prescribed value, $\Delta t \leq \frac{\text{LCFL}}{||\nabla \mathbf{u}||_\infty}$. In the case of rotors, we also impose that $\text{CFL}_{\text{tip}} = \frac{U_{\text{tip}}\,\Delta t}{h} \leq 4$. More

details on the VPM method and its theoretical foundation can be found in multiple reviews [37, 39, 40], and references therein. Additionally, a description of the present implementation on massively parallel architectures is provided in [38], based on the open-source PPM library [41].

2. Rotor modeling

The aerodynamics of rotor blades are modeled using immersed lifting lines (ILL). The lift and drag of each section of the line are retrieved from the locally computed effective velocity $\mathbf{U}_e$, the corresponding angle of attack, and user-provided 2D airfoil tables. The local bound circulation $\mathbf{\Gamma}_b$ is then computed from the Kutta-Joukowski equation,

$$\boldsymbol{\ell} = \rho \mathbf{U}_e \times \mathbf{\Gamma}_b, \tag{6}$$

where $\boldsymbol{\ell}$ is the sectional lift vector. The shed vorticity is then computed based on the spatial and temporal variations of the bound circulation, and introduced in the flow through the addition of particles. For brevity, we refer the reader to [42] for a detailed description of the ILL model.

In the VPM simulation presented in this paper, the ILLs are fed with airfoil tables corresponding to the 2D profiles used on the blades under investigation. These airfoil tables, formatted as standard `c81` files, describe the lift and drag coefficient as a function of Reynolds number and angle of attack, obtained experimentally.

The VPM method has a long history of verification and validation, including fundamental vortex dynamics [43] and engineering applications such as wind turbine wakes [44]. Multiple rotorcraft applications have recently been explored with the VPM method [45, 46], including validation of rotor loads in hover [47] and edgewise flight [48].

3. Wall boundary conditions

The presence of a solid wall such as the ground plane or the building walls is here accounted for using three different techniques to handle the corresponding boundary condition (BC). Part of this work is dedicated to comparing the results obtained with each technique.

The first one consists of a non-penetration, slip BC (later simply called "slip condition"). This condition is easily obtained in vortex methods using the method of images. All the vorticity in the computational domain is symmetrized with the ground plane acting as the symmetry plane. Doing so results in canceling the through-velocity component at the wall. In the present work, the image plane is implemented with a symmetric BC directly enforced at the wall by selecting the proper discrete sine/cosine transform in the Poisson solver.

The second BC is a non-penetration, no-slip condition (hereafter referred to as "no-slip"). Starting with the velocity field obtained with the slip condition, this condition amounts to modifying the finite difference stencils at the wall to impose a no-slip BC. A non-zero wall-vorticity is computed so that the velocity effectively goes to zero at the wall. More details on the implementation of this condition are presented in [22] along with validation results.

The third technique is based on the penalization method *à la* Brinkman [49]. The capabilities of this technique were recently illustrated in the context of medium-fidelity rotorcraft modeling for the simulation of rotorwash [18] and rotor-airframe interactions [48]. Penalization is used to force the local velocity of the fluid $\mathbf{u}$ to go to zero inside a prescribed volume. In theory, this is enforced through the addition of a penalization term to the momentum equations. In practice, the penalization operator is split from the rest of the Navier-Stokes operations and applied sequentially over the course of a time step. A correction on the velocity field is calculated as

$$\Delta\mathbf{u} = \mathbf{u}^* - \mathbf{u}^n = -\chi\,\mathbf{u}^n, \tag{7}$$

where the superscript n denotes the field at the n^{th} time step, the superscript $*$ denotes the penalized field, and χ is a mask function equal to 1 inside the penalized region and 0 elsewhere. Since vorticity is a primary variable of the solver, we compute the corresponding correction obtained as

$$\Delta\boldsymbol{\omega} = \boldsymbol{\omega}^* - \boldsymbol{\omega}^n = \nabla \times (\Delta\mathbf{u}). \tag{8}$$

The corrections, Eqs. (7) and (8), are added to the grid velocity and vorticity fields, respectively, at the beginning of every sub-time step. The remainder of the sub-step is performed "as usual" by computing the right-hand side of the Navier-Stokes equation using finite differences on the grid, acting on penalized vorticity and velocity. More details on the penalization method for vortex methods can be found in [50, 51].

IV. Computational Setup

A. Rotor geometry and operating conditions

We consider the rotor geometry of the NASA quadcopter urban air taxi concept (Fig. 2) described in Refs. 29, 30. A summary of the rotor properties is provided in Table 1, together with the parameters of the two operating conditions considered in this work. The rotor has three blades. Each blade is straight, linearly tapered, and equipped with modern thick airfoils. The blade twist is also linear, with $\theta = \Delta\theta(\frac{r}{R} - 0.75)$. The high-fidelity model of the rotor includes a rotor hub. It is not included in the medium-fidelity simulations.

All simulations are run with prescribed kinematics in both the medium- and high-fidelity frameworks. That is, the response of the blade to varying loads is neglected. Instead, the pitch and flap angles are kept constant throughout the simulations, and the same values are used for the isolated rotor and the quadrotor configuration. The flap angle is set arbitrarily to 0°. No airframe is included in any of the simulations; we leave the study of rotor-airframe-ground interactions for subsequent work.

Table 1 Rotor geometry and operating conditions.

Geometry		
tip radius R	2.81	[m]
root cutout R_i/R	0.12	[−]
thrust-weighted solidity σ	0.0647	[−]
blade twist difference $\Delta\theta$	−12.0	[°]
blade taper ratio $c_{\text{tip}}/c_{\text{root}}$	0.81	[−]
Operating conditions		
rotation rate Ω	570.0	[RPM]
blade collective pitch angle θ_0	10.0	[°]
blade coning angle β_0	0.0	[°]

B. High-fidelity setup

Two configurations are investigated with the isolated rotor: a flat ground and above a rooftop edge. In both cases, the rotor grids are recycled from our previous study in [30]. The grids for the flat ground case, shown in Fig. 4, are also identical to our previous study in [22]. When assembled, the final set of grids contains approximately 439 million points. We refer the reader to the latter publication for more details. The following paragraphs detail how the grids are constructed for the rooftop case.

The building is modeled with two semi-infinite flat surfaces. Three NB grids are used in the near-wall region: one for the horizontal ground (i.e., the rooftop), one for the vertical wall, and one for the edge (Fig. 5). The grids are stretched in the wall-normal direction so that the simulation maintains $y^+ < 1$. Smoothing is also applied to the edge grid to improve orthogonality. The remainder of the computational domain is made up of a set of partially overlapping background off-body (OB) grid. They are manually constructed to feature a wake-refinement region in the vicinity of the rotor, where a uniform grid size corresponding to 10% of the blade tip chord is used. This wake-refined region covers 1.5 radii above the ground surface and to the right of the vertical wall (in the $+z$ and $+x$ directions). A uniform resolution is maintained for the first 4 radii in $-z$ and $-x$, and laterally in the region $-1.5 < y/R < 1.5$. At larger distances, the resolution is decreased in a geometric progression until the outer BC is reached at about 20 rotor radii. Characteristic outflow conditions are utilized on the six outer faces of the background grid. The cut-hole technique in OVERFLOW-D mode enables blanking of the background mesh in the regions close to the rotor and to the building, where a no-slip condition is imposed at the wall. A sufficient grid overlap is maintained so that the solved quantities can be interpolated back and forth between the overset grids. The total number of grid points in the rooftop case is 448 million.

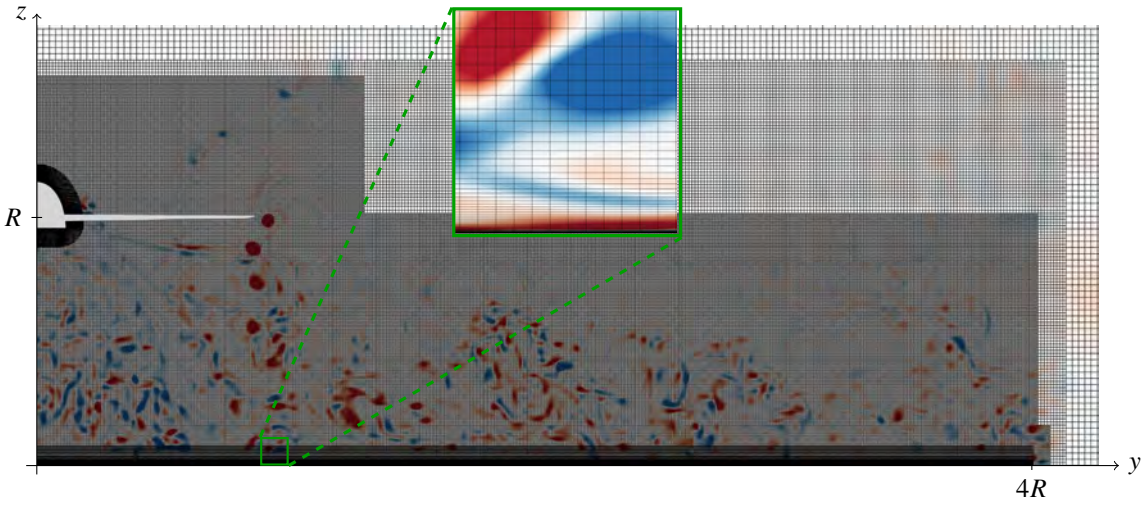

Fig. 4 Cut through the OVERFLOW mesh superimposed with an instantaneous snapshot of the vorticity ω_x. Besides the NB grids for the rotor, a separate NB grid is used at the wall with stretching in the wall-normal direction. The area between the rotor and the wall and the direct vicinity of the rotor are covered with fine grids of size $0.1c_{\text{tip}}$, to resolve the rotorwash. Outside of this wake-refined region and farther than four radii away from the rotor, OB grids are progressively coarsened until the outer BC is reached [22].

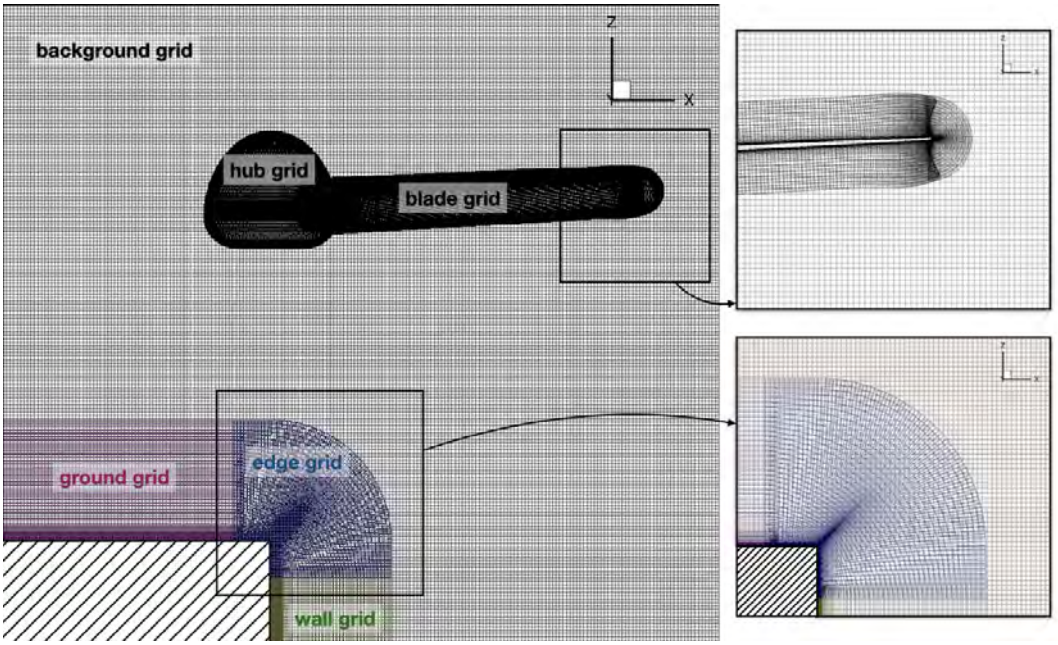

Fig. 5 Overset grids used for the OVERFLOW simulations of a single rotor IPGE.

C. Medium-fidelity setup

All VPM grids are Cartesian, i.e., with a uniform resolution. Only one resolution is used for the flat ground case in this paper. Our previous work [22] identified that a resolution of 48 grid points per rotor radius provided a good trade-off between accuracy and computational intensity. On the other hand, grid sensitivity is assessed for the rooftop case by comparing the results of VPM simulations at three different spatial resolutions, from 32 to 64 points per radius.

The simulations of the single rotor cases IGE above a flat ground are performed in a domain of size $6D \times 6D \times 2D$. The rotor is centered in the domain in x and y, and is placed at one rotor radius above the ground in z. Different simulations are carried out using the three wall BCs available in the current VPM implementation. Note that none of

them are intended to fully capture the wall boundary layer. A proper no-slip wall would require a much finer resolution for the range of Reynolds numbers at hand. Instead, our simulations are utilized as a model of the inviscid and viscous ground. Comparison with the high-fidelity CFD will allow us to verify the quality of this modeling approach.

In the case of the single rotor IPGE above the rooftop edge, a penalization region is imposed for all x, z such that $x < 0$ and $z < 0$. The simulation domain covers the area $[-5R, 4R] \times [-4R, 4R] \times [-5R, 3R]$ and the rotor is located at $(0, 0, 1R)$. The configuration is similar for the quadrotor IPGE, but the domain boundaries are extended to $[-8R, 6R] \times [-6R, 6R] \times [-8R, 4R]$ and the rotors are placed at $(\pm 1.35R, \pm 1.35R, 1R)$.

For both geometries, unbounded BCs are used for all the boundaries that do not coincide with a wall. More details on the BCs in the VPM method and their implementation are discussed in [33].

V. Single Rotor in Ground Effect over a Flat Ground

This section considers a single rotor in ground effect. We assess the quality of the outwash predictions obtained with different wall BCs in the VPM computation by comparing them with reference DDES results. The boundary conditions that are investigated are: a slip BC, a coarsely-resolved no-slip BC and a penalized boundary. Implementation details are provided in Section III.B.3. The goal here is to quantify the accuracy of the VPM predictions compared to the OVERFLOW reference, where the wall boundary layer is calculated accurately.

Table 2 List of single rotor IPGE simulations.

label	h	$\frac{t_{\text{end}}}{T_{\text{rev}}}$	$\frac{360\Delta t}{T_{\text{rev}}}$ *
VPM-Slip	$R/48$	100	7.2°
VPM-NoSlip	$R/48$	100	5.4°
VPM-Pena	$R/48$	100	3.6°
OVERFLOW	$c_{\text{tip}}/10$	40	0.25°

* VPM time step is adaptive. The value shown is an average.

Table 2 lists the simulations that are analyzed and reports the main computational parameters along with the physical time reached at the end of the simulations t_{end}. For the VPM runs, the uniform spatial resolution of 48 points per radius is selected as our previous experience with a similar configuration showed it provides a favorable trade-off between computational intensity and accuracy. The grid spacing indicated for the OVERFLOW simulation corresponds to the resolution employed in the wake-resolved region.

Note that, since the VPM method runs faster than OVERFLOW, it was possible to reach 100 rotor revolutions of age in the VPM simulations. However, due to practical constraints in the schedule of the present writing, the OVERFLOW reference simulation is limited to 40 rotor revolutions of age. We demonstrated in [22] that this duration is sufficient for the starting structures of the simulation to evacuate the domain, allowing us to examine the established flow.

A. Time-averaged flow

The time-averaged flow field is shown in Fig. 6, as a result of the VPM-NoSlip simulation. As described in previous research [4, 7], the flow can be subdivided into different regions. The region directly beneath the rotor is dominated by the downwash of the rotor and is characterized by a contraction of the vein emanating from the rotor. Closer to the wall, the downwash transitions to outwash as the flow entrained by the rotor is deviated radially by the wall. Subsequently, a jet forms along the wall in the outwash region.

Our previous work suggested that obtaining converged flow statistics requires averaging periods longer than 10 rotor revolution periods, after the initial transient associated with starting vortices has evacuated the region of interest. Therefore, all the flow averages presented hereafter are calculated using an averaging period corresponding to the last 10 rotor revolutions in the OVERFLOW simulations and the last 25 rotor revolutions in the VPM simulations. Averaging is discussed in further detail in [22].

B. Outwash

Velocity profiles are shown in Fig. 7, normalized by the reference induced velocity of the rotor. The agreement between all simulations is generally good, including with the reference OVERFLOW simulation. However, some

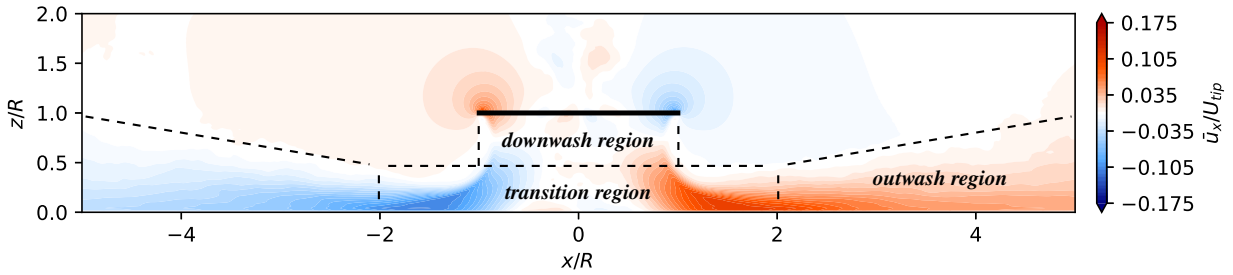

Fig. 6 Time-averaged outwash velocity ($\bar{u}_x$) induced by the rotor hovering at one radius above the ground in the VPM-NoSlip simulation, averaged over the last 25 revolutions.

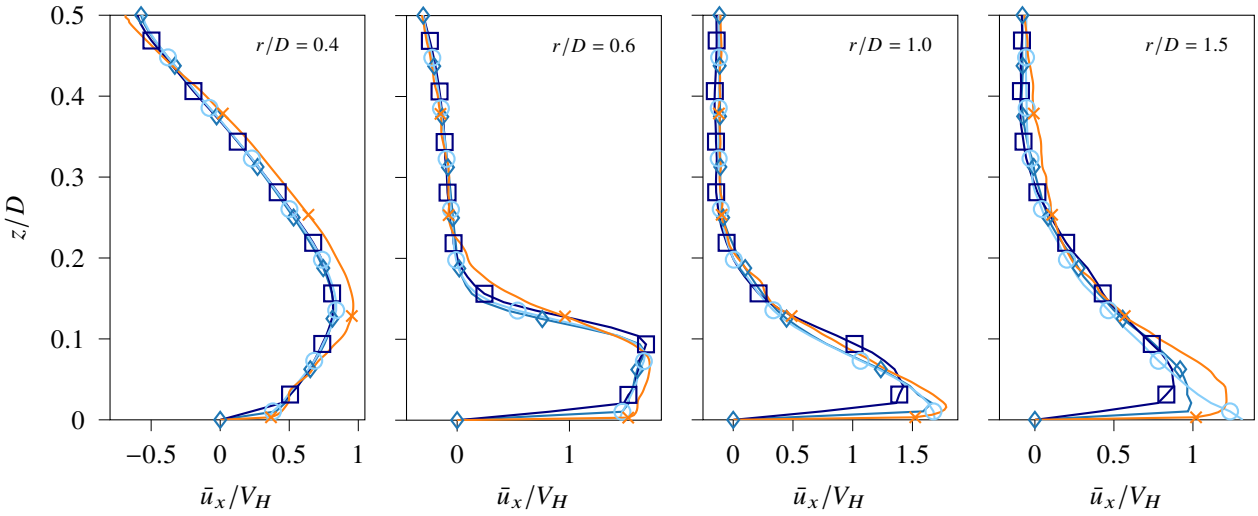

Fig. 7 Outwash velocity profile at increasing radial locations for OVERFLOW ( ), VPM-NoSlip ( ), VPM-Pena ( ) and VPM-Slip ( ). For readability, markers are not drawn at every data point.

discrepancies are noticeable, particularly in the wall jet at $r/D \geq 1.0$. The slip condition obviously does not constrain the outwash velocity at the wall, which results in a monotonically increasing velocity in the jet. On the other hand, the results obtained with the no-slip BC more closely reproduce the trends of the reference OVERFLOW velocity profiles, even though there is an undershoot at large r/D. The penalization BC results in a velocity profile with an even smaller maximum velocity but nonetheless captures the correct trends.

Recall that the VPM resolution is clearly too coarse to properly resolve the wall boundary layer. The use of the coarsely-resolved boundary layer is therefore intended as a model to capture the effect of the ground on the outwash flow. The above comparison demonstrate that both no-slip and penalization conditions can produce satisfactory outwash velocity profiles. However, we note that the former performs slightly better.

In addition to diagnostics based on the average velocity field, the velocity fluctuations are examined through the profile of the standard deviation of the velocity presented in Fig. 8. The fluctuation of each velocity component is calculated as $\mathbf{u}' = \mathbf{u} - \bar{\mathbf{u}}$, and the standard deviation as $u_{\text{std}} = \frac{1}{3}\left(\overline{u_x'^2} + \overline{u_y'^2} + \overline{u_z'^2}\right)^{1/2}$. High fluctuations are detrimental to the safety of a person immersed in a rotorwash [4].

All simulation results compare generally well. In particular, the different VPM methods are able to reproduce the trends that the OVERFLOW profiles exhibit. Once again, this is quite remarkable, considering that none of the VPM simulations is fine enough to properly capture the wall boundary layer.

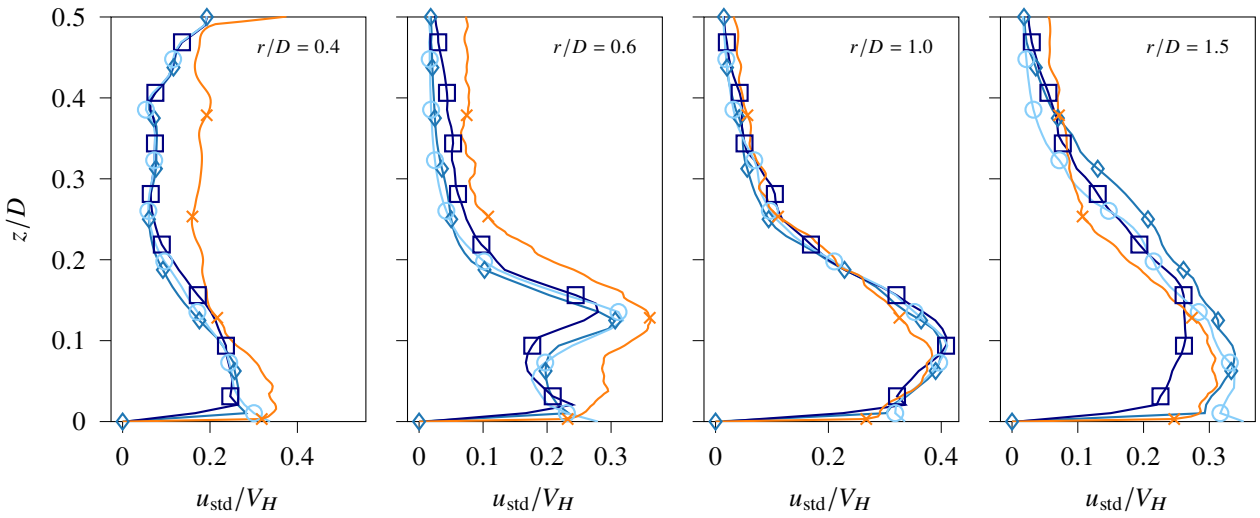

Fig. 8 Velocity fluctuations in the wall jet at increasing radial locations for OVERFLOW ( ), VPM-NoSlip ( ), VPM-Pena ( ) and VPM-Slip ( ).

C. Rotor loads

The distribution of the blade normal force coefficient is calculated by averaging the loading on the blade over a period corresponding to five rotor revolutions. The results are shown in Fig. 9. The VPM results agree well with the reference OVERFLOW simulation regardless of the wall BC, except in the tip region. Previous experience with the ILL model implemented in the VPM solver [22, 47] has shown that this behavior is caused by the difficulty for the ILL to accurately predict the blade-vortex interaction (BVI). The effect of the preceding tip vortex on the blade is not fully captured because the model misses the details associated with the local three-dimensionality of the flow at the chord-size scale. However, we note that the model correctly predicts the trends in the loading, with a peak in the loading towards the tip.

Among the three BCs, the loadings obtained with the slip and no-slip BCs are almost identical. The penalization yields very similar values as well. This suggests that the rotor loading is not so sensitive to the details of the flow near the ground, provided that it operates outside the wall boundary layer.

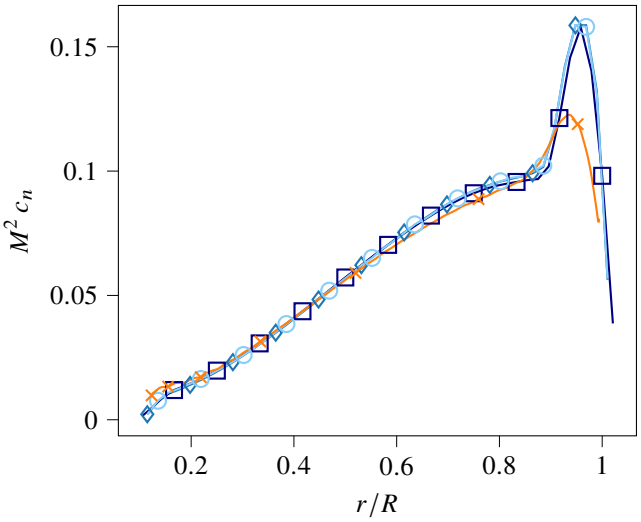

Fig. 9 Blade normal loads on the single rotor IGE at $H/R = 1$ for OVERFLOW ( ), VPM-NoSlip ( ), VPM-Pena ( ) and VPM-Slip ( ).

VI. Single Rotor in Partial Ground Effect over a Rooftop Edge

The second case investigated in this work considers an isolated rotor located above the edge of the building ($x = 0$) at a height of one radius. Results are obtained with OVERFLOW and with the VPM method. However, because of time constraints, it was not possible to obtain sufficiently converged flow statistics from the OVERFLOW-IPGE computation. Only the rotor loads could be obtained with a satisfactory degree of statisical convergence, and we limit the code-to-code comparisons to that quantity in this preliminary study. Future work will extend the comparisons to the flow field.

The VPM simulations utilize the penalization BC for the building walls, and three different resolutions: VPM-Pena-32, VPM-Pena-48, VPM-Pena-64. The last to digits indicate the number of grid points per radius in each case. The slip and no-slip BCs rely on a symmetry condition that can only be applied to a flat surface.

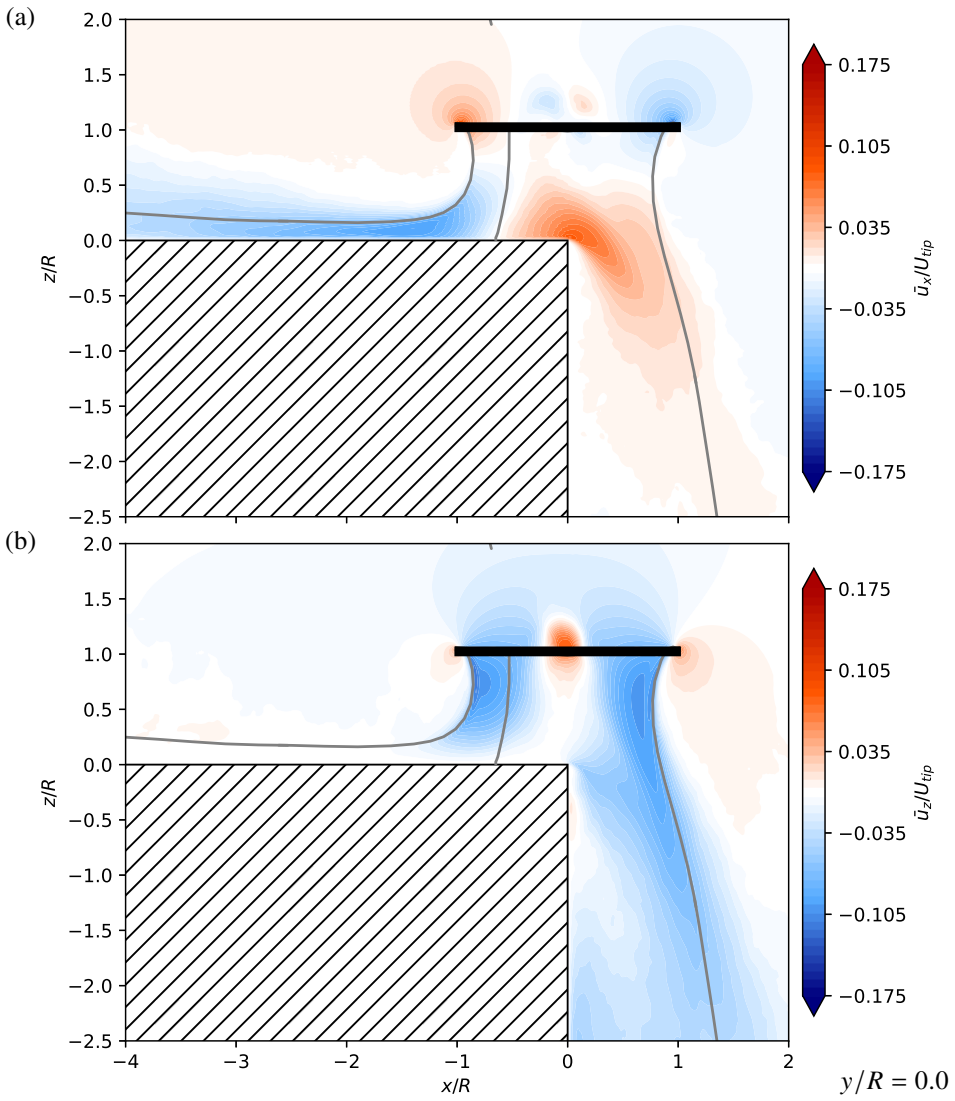

Fig. 10 Time-averaged (a) horizontal velocity and (b) vertical velocity induced by the rotor hovering at 1R above the ground, computed from the VPM-Pena-64 simulation, with streamtraces starting from the blade tips in gray.

A. Time-averaged flow

The time-averaged flow field from the VPM simulation in a cross section normal to the edge of the building and centered on the rotor is shown in Fig. 10. Towards the horizontal surface, the observed flow features are very similar to the case of hover in ground effect, with a wall jet forming. However, a stagnation point exists on the wall that is not exactly below the rotor shaft, as was the case in the IGE configuration. As a result, the flow vein that passes through the rotor is divided into two streams. The first one undergoes a transition similar to the flat ground case and creates the wall jet on the building rooftop. Note that the dividing streamline that connects the rotor to the stagnation point on the horizontal surface is also offset towards the negative x. As a result, we expect the jet to entrain less flow compared to the case of the IGE rotor. The other part of the stream on the right-hand side of the dividing streamline flows down along the vertical wall. The flow separates at the edge and creates a recirculation region at the top of the vertical wall, forcing the main stream to go around it. Eventually, there is reattachment around $z/R = -1.0$.

B. Outwash and downwash

Figure 11 presents the average outwash profiles calculated along the normal to the horizontal wall. Similar features can be observed as in the IGE case. Figure 12 shows the downwash profiles along the normal to the vertical wall. The flow separation at the building edge and the ensuing recirculation is evidenced by the presence of small or negative velocity values close to the wall at $z/R < 0$. The downwash velocity peaks at increasingly high distances in z as the flow deviates in an oblique fashion. This could be already observed in Fig. 10 where the distance between the vertical wall and the right-most streamline increases along the $-z$ direction.

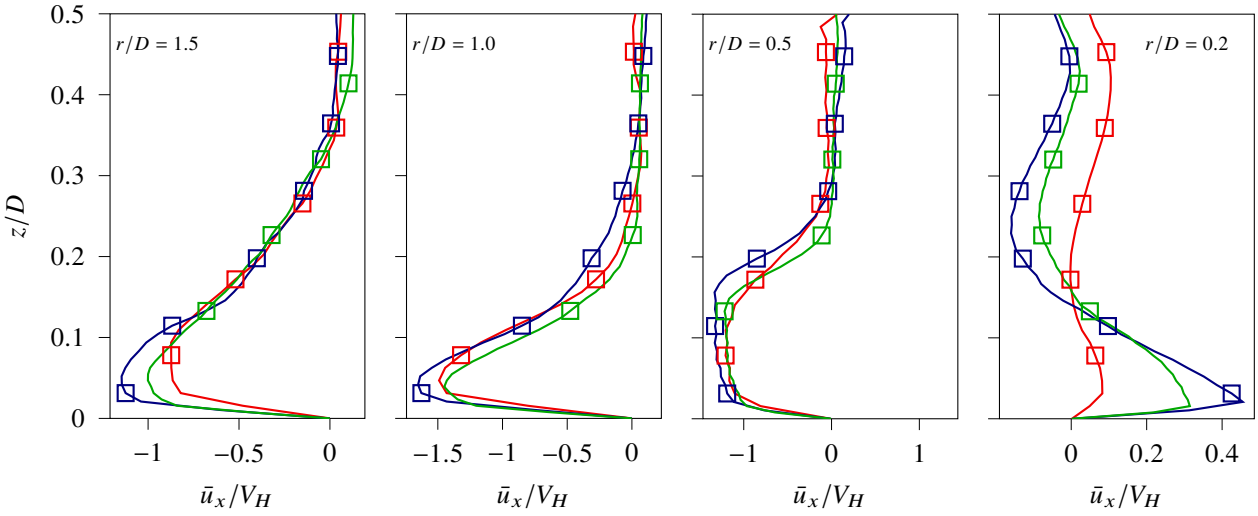

Fig. 11 Outwash velocity profile calculated along the normal to the horizontal wall at increasing radial locations in the plane $y = 0$ for VPM-Pena-32 ( ), VPM-Pena-48 ( ), and VPM-Pena-64 ( ).

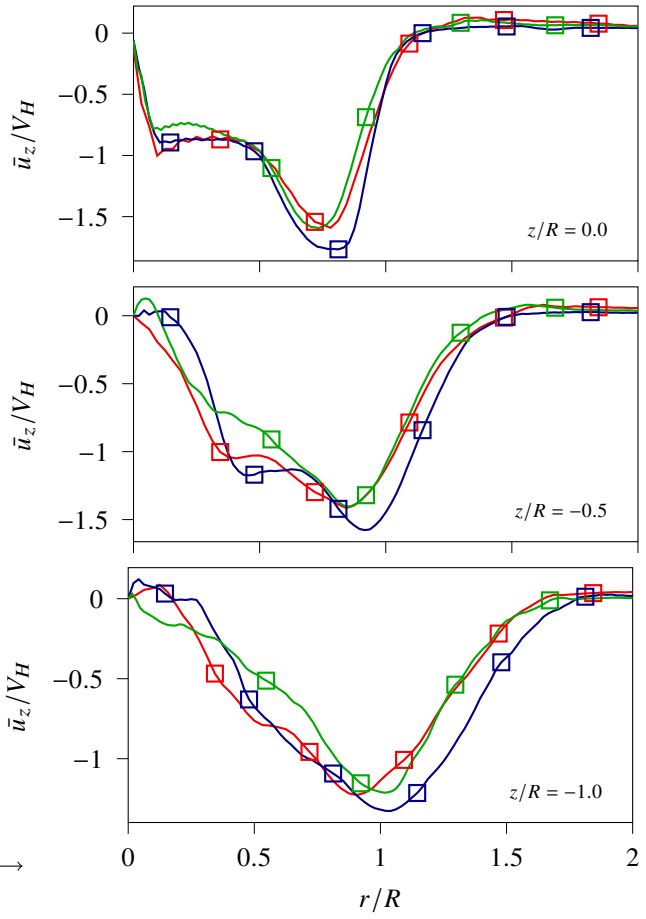

Fig. 12 Downwash velocity profile calculated along the normal to the vertical wall at downstream distances in the plane $y = 0$ for VPM-Pena-32 ( ), VPM-Pena-48 ( ), and VPM-Pena-64 ( ).

For both outwash and downwash, the effect of the mesh resolution on the results is non-trivial, as no "convergence" can be observed *per se*. Nevertheless, the results generally exhibit a relatively small sensitivity to the grid resolution, with a maximum absolute difference of about $0.2V_H$ at the peak. This will be further discussed in the next section.

To compare the properties of the wall jet between the full IGE case and the IPGE case, Fig. 13 shows the maximum outwash velocity across the height as a function of the distance to the edge of the building. It can be seen that, despite the lateral offset of the separation point in the IPGE case, the establishment of the wall jet is similar to the IGE case, as measured by the location where $\bar{V}_{\max}$ is minimum. When normalized by the reference induction of the rotor, the maximum velocity in the wall jet is smaller in the IGE case. However, V_H is a linear function of thrust which is higher in the latter case, as discussed in the next section.

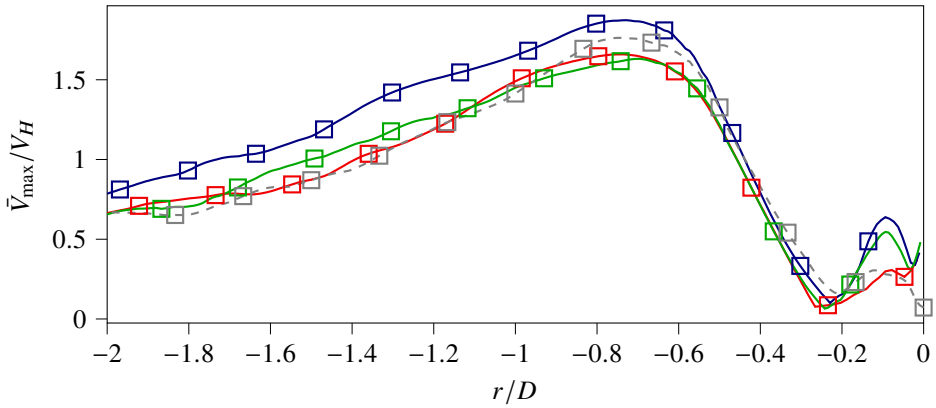

Fig. 13 Maximum outwash velocity as a function of the radial distance calculated in the plane $y = 0$ for the single rotor IPGE with VPM-Pena-32 ( ), VPM-Pena-48 ( ), and VPM-Pena-64 ( ). The outwash velocity in the full IGE case computed with VPM-Pena-48 ( ) is also shown.

C. Distributed loads

Due to the asymmetry in the geometry, the rotor blades experience a time-dependent ground effect, resulting in periodic loads. We recall that, for simplicity, the present simulations ignore the flapping response of the blade to the time-varying loads.

First, comparisons of the time-averaged sectional normal load coefficient are shown in Fig. 14 with plain averaging over the last 10 rotor revolutions of each simulation. The reference loadings obtained with OVERFLOW in the IGE and OGE cases are also shown. Since the IPGE case is somehow combining the IGE and OGE configurations, one might expect that the IPGE average loading amounts to the average between the two. Considering only the OVERFLOW results to begin with, we notice that the IPGE loading is rather close to the OGE loading on the innermost 80% of the radius. This correlates with our previous observation that most of the flow going through the rotor continues downwards along the vertical wall (see our discussion on the dividing streamline). The effect of blockage by the horizontal wall is thus limited in the inner portion of the rotor that operates close to the OGE case. However, the peak in normal loading at the tip reflects the IPGE configuration as its amplitude (≈ 0.030) is between the values calculated for the OGE peak (≈ 0.045) and the IGE peak (≈ 0.025). As observed in our previous work [22], the amplitude of the peak is indeed larger in the OGE case due to a tip vortex trajectory that penetrates more inboard below the rotor, compared to the IGE case.

The effect of mesh resolution on the VPM results is similar to what was observed in full ground effect in our previous work [22]. While minor differences are observed over the inner portion of the blade radius, the tip region exhibits the largest discrepancies. Of note, the amplitude of the peak correlates with the maximum outwash and downwash velocities reported in the previous section, with lower peaks being associated with larger velocities. This suggests a strong dependence of the wall jet properties on the flow characteristics in the tip region, which is also generally where the downwash velocity is the largest. However, as mentioned previously, the ILL is not equipped to accurately model blade-vortex interaction. Even though the trends in the loading are correctly captured, inconsistent predictions of the tip loads lead to the amplitude of the peak being overestimated.

The periodicity of the normal loads is illustrated in Fig. 15 which shows a polar representation of the phase-averaged sectional normal force coefficient for a single blade. Phase averaging is done over 10 rotor revolutions. The inner part of

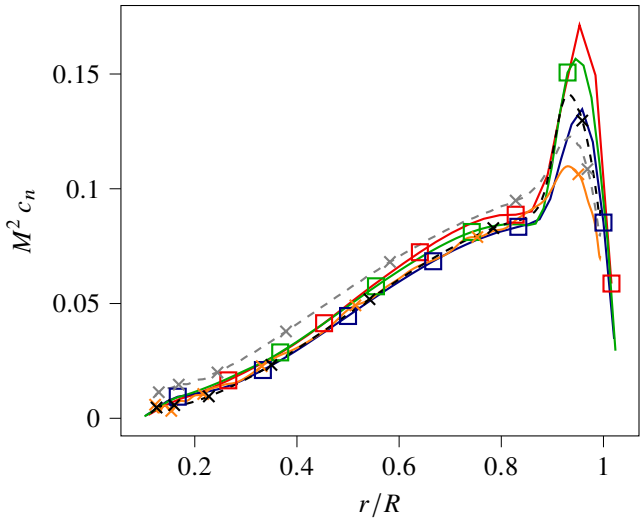

Fig. 14 Time-averaged radial distribution of the normal loads on a single rotor IPGE obtained with VPM-Pena-32 ( ), VPM-Pena-48 ( ), VPM-Pena-64 ( ), and OVERFLOW ( ). The distribution for the OGE case ( ) and the full IGE case ( ) obtained with OVERFLOW are also shown.

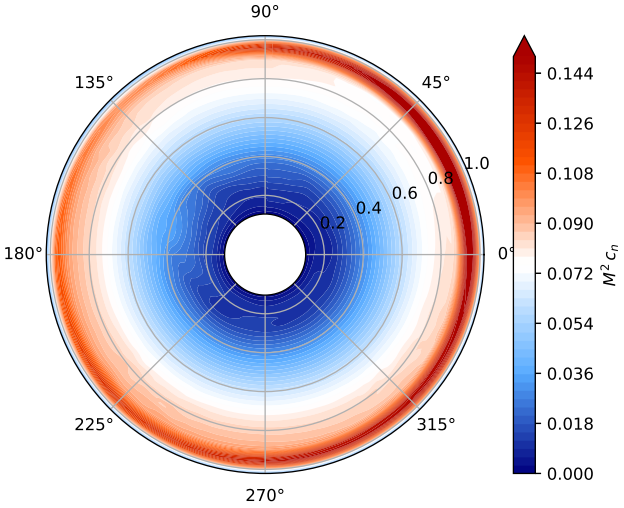

Fig. 15 Phase-averaged distribution of the normal load coefficient over the rotor disk IPGE obtained with VPM-Pena-48.

Table 3 Thrust and moments on the single rotor in different configurations.

solver	case	h	$\mathcal{T}/\mathcal{T}_{\text{ref}}$	$\mathcal{M}_x/\mathcal{M}_{\text{ref}}$	$\mathcal{M}_y/\mathcal{M}_{\text{ref}}$
OVERFLOW	IPGE	$c_{\text{tip}}/10$	1.02	−0.028	−0.091
OVERFLOW	IGE	$c_{\text{tip}}/10$	1.12	−0.003	−0.003
VPM-Pena-32	IPGE	$R/32$	1.02	−0.016	−0.019
VPM-Pena-48	IPGE	$R/48$	0.90	−0.013	−0.014
VPM-Pena-64	IPGE	$R/64$	0.99	−0.003	−0.011
VPM-Pena-48	IGE	$R/48$	1.08	< 0.001	< 0.001

the blade features a mostly axisymmetric loading, again evidencing the limited effect of blockage in this region. On the other hand, the tip loading is markedly periodic, with a lower peak loading when the blade passes above the building in the range of azimuthal angles $90° < \psi < 270°$. This is consistent with the effect of the ground calculated in the OGE and IGE simulations, with lower peak amplitude in the latter case.

D. Integrated forces and moments

The asymmetry in normal loading creates an aerodynamic moment at the rotor hub. Table 3 shows relative comparisons in the total thrust and moment coefficients of the rotor. The relative increase in thrust is normalized with the thrust of the OGE case, $\mathcal{T}_{\text{ref}} = \mathcal{T}_{\text{OGE}}^{\text{single}}$. The aerodynamic moment is normalized with a reference value $\mathcal{M}_{\text{ref}} = R\,\mathcal{T}_{\text{ref}}$. Moments are calculated with respect to the center of the rotor.

The thrust calculated with OVERFLOW reflects the observation of the previous section with the IPGE value being only 2% higher than the OGE thrust, whereas the full IGE case leads to a 12% increase. The values obtained using the VPM vary substantially due to the tip load prediction issue, although the predicted IGE thrust is indeed higher than the IPGE thrust.

Moment values are reported as an indication of the rotor imbalance that originates in the partial ground effect. We note that neglecting the blade flapping response does not lead to realistic rotor aeromechanics. Therefore, only relative comparisons are made. The moments calculated in the IGE case should be zero. The residual values shown in the table

are indeed small and originate in averaging over a finite number of revolutions. The largest moment is obtained in the IPGE case computed with OVERFLOW. The sign of this moment is negative, that is, it would cause the rotor to tilt towards the building. This is rather counterintuitive, as one might have expected that the partial ground effect would increase the loads on the side of the rotor located over the building, hence creating a positive, repelling moment. The negative value is here due to the behavior of the normal load at the blade tip which is in fact lower when the blade passes above the building, as explained in the previous section.

The sign of the moments computed with the VPM method agree with the OVERFLOW values, which again illustrates that the VPM simulations capture the correct trends. However, their magnitude varies substantially with the mesh resolution. Compared to thrust, the effect of incorrect tip loads is amplified in the moment computation. Therefore, due to the current limitations of the ILL model, the VPM values cannot be accurate.

To conclude this section, we emphasize the need for further validation of the IPGE case with dedicated experimental results to consolidate the above discussions. This will be considered in future work for which converged flow statistics computed with OVERFLOW should also be available for comparison. Additionally, dedicated modeling of the BVI should be introduced in the ILL technique to improve the accuracy of tip load predictions.

VII. Quadrotor in Partial Ground Effect over a Rooftop Edge

In this section, preliminary results for the quadrotor vehicle in partial ground effect are examined. Only one simulation is performed with the VPM method, again with a resolution of 48 particles per rotor radius.

The geometry of the representative building is the same as in the single rotor case. The four rotors are all located in a horizontal plane at a height of $H/R = 1.31$ above the rooftop surface. They are placed to mimic the design of NASA's urban air taxi concept with a lateral spacing such that the hub of each rotor is located at $x/R = \pm 1.35$ and $y/R = \pm 1.35$. The airframe of the taxi is not incorporated in the simulation.

Figure 16 shows an instantaneous snapshot of the 3D vorticity field obtained at the end of the IGE, IPGE, and OGE simulations. In the IGE case, large vortical structures fill the gap between the rotors and are eventually ejected radially in the $\pm x$ and $\pm y$ directions, as highlighted in [22]. These structures originate in portions of the blade tip vortices that get trapped between the four rotors. A similar phenomenon occurs in the IPGE case, although only along the horizontal wall in the $-x$ direction. The region between the other rotors (in the $+x$ and $\pm y$ directions) remains clear of large coherent structures. Since the blockage introduced by the building is only partial, most of the tip vortices are advected downward along the vertical wall.

This behavior is further illustrated with the time-averaged velocity computed in a cross-section shown in Fig. 17. The airflow entrained through each rotor is materialized with the streamtraces starting at the blade tips. Part of the stream that traverses the rotor located above the building passes around the edge of the building and meets the stream that originates from the other rotor. This allows the tip vortices to "leak" along the wall. Also, as a result of the interaction between the two streams, the downwash region below the rotor on the right in the figure is shifted towards the wall. Therefore, one can expect the loads on the left and right rotors to be similar to the IGE and OGE cases, respectively. However, as shown in the previous section, the tip loads are affected by the actual trajectory of the tip vortices, which here differ slightly from the IGE and OGE cases.

Finally, the effect of the partial ground effect on the vehicle is studied by examining the total thrust of the vehicle, reported in Table 4. Moment values are not reported since they are inaccurate due to the tip load prediction issue, as discussed previously. The total thrust of the quadrotor OGE is less than four times the thrust of the isolated rotor, due to rotor-rotor interactions. The IGE case features an increase in thrust, although it is relatively smaller than the increase obtained for the single rotor. As expected, the thrust of the IPGE case lies between the IGE and OGE values. The current limitation associated with the tip load predictions in the ILL model should be overcome before further analysis can be made.

Table 4 Thrust on the quadrotor in different configurations.

solver	case	$\mathscr{T}/\mathscr{T}_{\text{ref}}$
VPM-Pena-48	OGE	3.91
VPM-Pena-48	IPGE	4.06
VPM-Pena-48	IGE	4.12

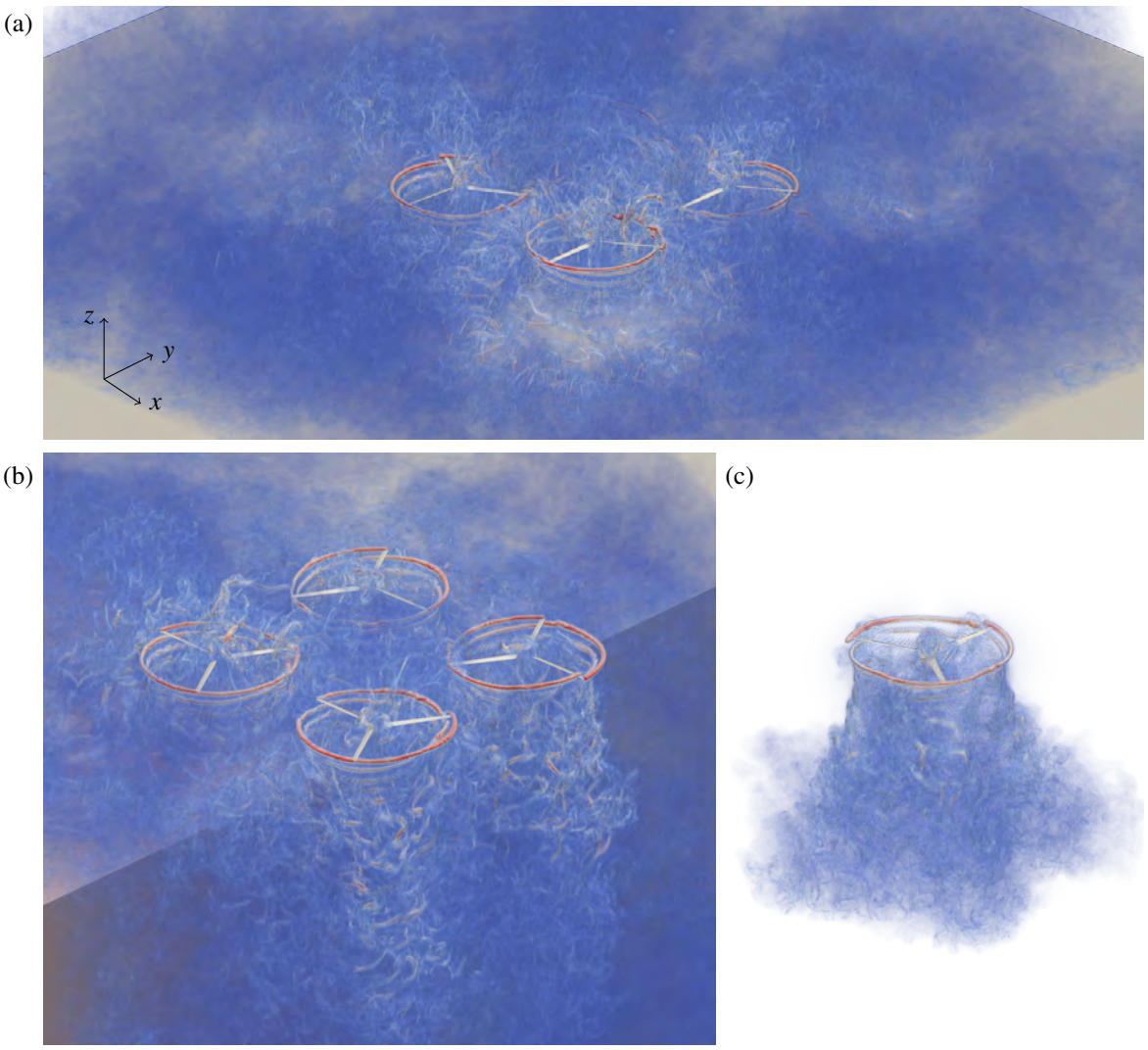

Fig. 16 Volume rendering of the instantaneous vorticity magnitude in the vicinity of (a) the quadrotor in full ground effect, (b) the quadrotor in partial ground effect, and (c) the single rotor out of ground effect.

VIII. Conclusions

This work considered the use of CFD for the analysis of rotorwash in full and partial ground effect. A single rotor was simulated IGE with the high-fidelity solver OVERFLOW and the medium-fidelity VPM method, and the simulations were compared to highlight the effect of various BCs to model the influence of the ground. The reference high-fidelity simulation was used to verify the consistency of the modeling approaches in the medium-fidelity solver. More comparisons were made for a single rotor operating IPGE. Finally, a quadrotor air taxi IPGE was simulated with the VPM method to quantify the load imbalance when the vehicle hovers above a rooftop edge.

The conclusions of this study are summarized as follows:

- High-fidelity DDES simulations can be used to verify the results obtained with lower-fidelity simulation tools on simple geometries. The latter tools can then be used to gain valuable insights in studies involving larger domains or multiple cases, owing to their smaller computational intensity.
- Favorable comparisons were obtained between the VPM method with immersed lifting lines and OVERFLOW. In the case of the single rotor IGE, the spanwise distribution of normal loads was correctly predicted over most of the blade, although discrepancies existed in the tip region due to a limitation of the model in computing the surge caused by the BVI. Regarding the various techniques that were investigated to account for the presence of a flat surface in the VPM method, the under-resolved no-slip BC was deemed the most accurate. The penalization BC

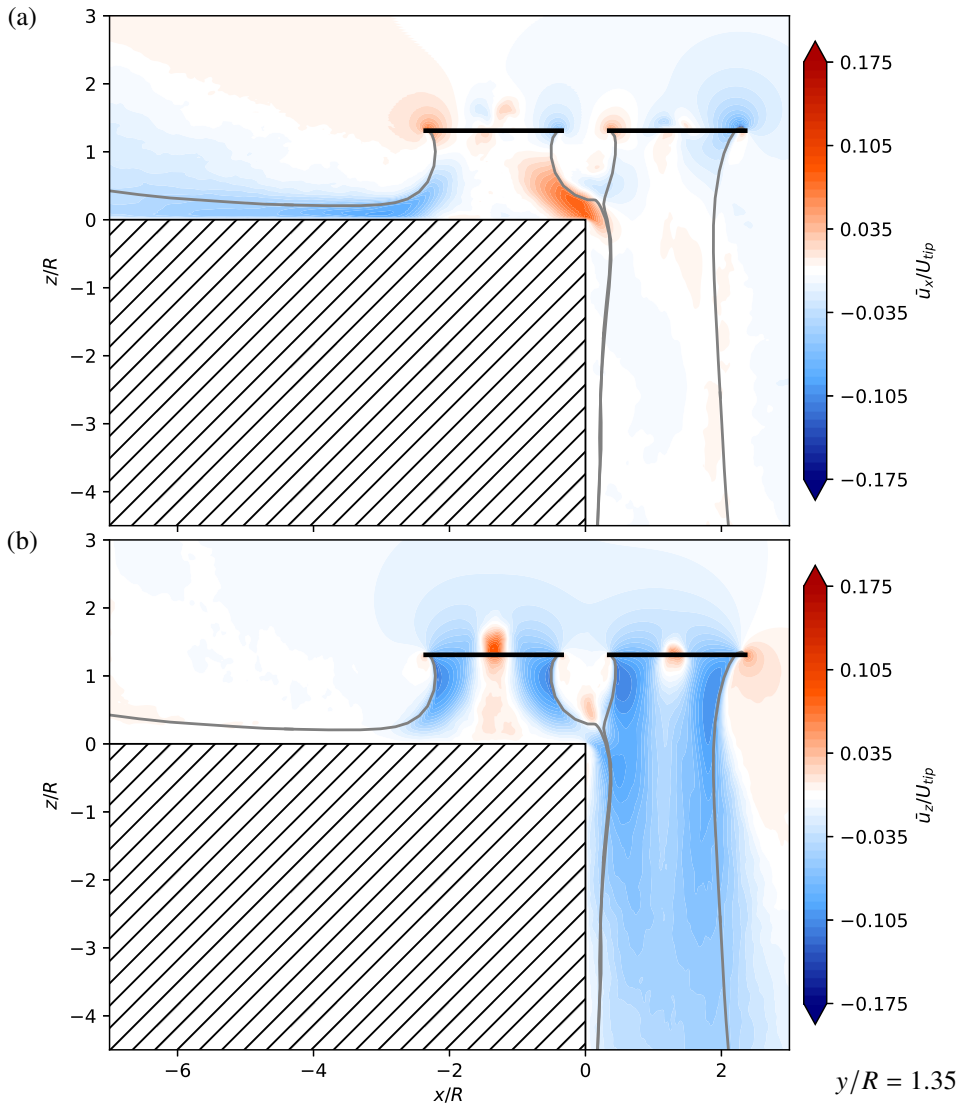

Fig. 17 Time-averaged horizontal velocity (a) and vertical velocity (b) induced by the quadrotor hovering at 1.31R above the building, computed from the VPM-Pena-48 simulation, with streamtraces starting from the blade tips in gray.

yielded less satisfactory results; however, it can be used in the case of non-flat surfaces. The no-slip BC was not able to reproduce the correct trends in the velocity field near the ground, due to the absence of wall friction.

- The time-averaged flow past the single rotor IPGE was analyzed. It was shown that most of the flow that pass through the rotor is advected downwards. As a result, the inner region of the rotor operates similarly to the OGE configuration. Still, a wall jet forms along the horizontal wall as in the IGE case, although with a maximum velocity in the wall jet approximately 20% larger (when normalized with their respective reference induced velocity). The asymmetry in ground effect is also responsible for a non-zero moment on the rotor that would cause it to tilt towards the building. This effect was consistently predicted in the VPM and OVERFLOW simulations.
- Additional insights into the flow and the loads in the case of a quadrotor IPGE were gained from a VPM simulation. In both the single rotor and quadrotor cases, the accurate computation of the tip loads was identified as crucial since it drives the rotor moments and induction. However, a current limitation of the immersed lifting line used to model the blade in the VPM simulation hampers accurate predictions of the blade-vortex interactions, hindering the accuracy of the results.

Although high-fidelity simulations were used as a reference for comparisons in this work, we insist that further

validations against experimental results are needed for both medium- and high-fidelity methods, especially in cases with geometries more complex than a single rotor.

IX. Acknowledgments

D.-G. Caprace is supported by an appointment to the NASA Postdoctoral Program at NASA Ames Research Center, administered by Oak Ridge Associated Universities under contract with NASA. Resources supporting this work were provided by the NASA High-End Computing (HEC) Program through the NASA Advanced Supercomputing (NAS) Division at Ames Research Center. The authors express their deep gratitude to Profs. Philippe Chatelain and Grégoire Winckelmans (UCLouvain, Belgium) for providing access to the source code of VPM4x.

References

[1] Visingardi, A., Fabrizio, D. G., Schwarz, T., Schmid, M., Bakker, R., Voutsinas, S. G., Gallas, Q., Boissard, R., Gibertini, G., Zagaglia, D., et al., "Forces on Obstacles in Rotor Wake-A GARTEUR Action Group," *43rd European Rotorcraft Forum*, 2017.

[2] Brown, R., "Are eVTOL aircraft inherently more susceptible to the vortex ring statethan conventional helicopters," *48th European Rotorcraft Forum*, Winterthur, Switzerland, 2022.

[3] Johnson, W., and Silva, C., "NASA concept vehicles and the engineering of advanced air mobility aircraft," *The Aeronautical Journal*, 2021, pp. 1–33. https://doi.org/10.1017/aer.2021.92.

[4] Preston, J. R., Troutman, S., Keen, E., Silva, M., Whitman, N., Calvert, M., Cardamone, M., Moulton, M., and Ferguson, S. W., "Rotorwash operational footprint modeling," Tech. Rep. RDMR-AF-14-02, US Army RDECOM, 2014.

[5] Lee, T. E., Leishman, J. G., and Ramasamy, M., "Fluid Dynamics of Interacting Blade Tip Vortices with a Ground Plane," *Journal of the American Helicopter Society*, Vol. 55, No. 2, 2010, p. 22005. https://doi.org/doi:10.4050/JAHS.55.022005.

[6] Tanner, P. E., Overmeyer, A. D., Jenkins, L. N., Yao, C.-S., and Bartram, S. M., "Experimental investigation of rotorcraft outwash in ground effect," *American Helicopter Society International Annual Forum & Technology Display*, 2015.

[7] Ramasamy, M., and Yamauchi, G. K., "Using Model-Scale Tandem-Rotor Measurements in Ground Effect to Understand Full-Scale CH-47D Outwash," *Journal of the American Helicopter Society*, Vol. 62, No. 1, 2017, pp. 1–14. https://doi.org/doi:10.4050/JAHS.62.012004.

[8] Dekker, H. N. J., Ragni, D., Baars, W. J., Scarano, F., and Tuinstra, M., "Aerodynamic Interactions of Side-by-Side Rotors in Ground Proximity," *AIAA Journal*, Vol. 60, No. 7, 2022, pp. 4267–4277. https://doi.org/10.2514/1.J061105.

[9] Ganesh, B., Komerath, N., Pulla, D. P., and Conlisk, A., "Unsteady Aerodynamics of Rotorcraft in Ground Effect," *43rd AIAA Aerospace Sciences Meeting and Exhibit*, 2005. https://doi.org/10.2514/6.2005-1407.

[10] Silva, M., abd Leighton Myers, E. H., Tritschler, J., and Holder, J., "Full-Scale Investigation of Rotor/Obstacle Interactions using an Elevated Fixed Platform," *Vertical Flight Society 78th annual forum*, Fort Worth, Texas, 2022.

[11] Pickles, D., Green, R., and Giuni, M., "Rotor wake interactions with an obstacle on the ground," *The Aeronautical Journal*, Vol. 122, No. 1251, 2018, pp. 798–820. https://doi.org/10.1017/aer.2018.7.

[12] Taymourtash, N., Zagaglia, D., Zanotti, A., Muscarello, V., Gibertini, G., and Quaranta, G., "Experimental study of a helicopter model in shipboard operations," *Aerospace Science and Technology*, Vol. 115, 2021, p. 106774. https://doi.org/https://doi.org/10.1016/j.ast.2021.106774.

[13] Hwang, J. Y., and Kwon, O. J., "Assessment of S-76 rotor hover performance in ground effect using an unstructured mixed mesh method," *Aerospace Science and Technology*, Vol. 84, 2019, pp. 223–236. https://doi.org/https://doi.org/10.1016/j.ast.2018.10.023.

[14] Narducci, R. P., and Hariharan, N. S., "A Common Simulation for Hover Validation of a Helicopter near the Ground," *AIAA Scitech Forum*, 2023. https://doi.org/10.2514/6.2023-1187.

[15] Ramasamy, M., Potsdam, M., and Yamauchi, G. K., "Measurements to understand the flow mechanisms contributing to tandem-rotor outwash," *Ameriacan Helicopter Society 71st annual forum*, 2015.

[16] Chirico, G., Szubert, D., Vigevano, L., and Barakos, G. N., "Numerical modelling of the aerodynamic interference between helicopter and ground obstacles," *CEAS Aeronautical Journal*, Vol. 8, No. 4, 2017, pp. 589–611. https://doi.org/10.1007/s13272-017-0259-y.

[17] Merabet, R., and Laurendeau, E., "Numerical simulations of a rotor in confined areas including the presence of wind," *Aerospace Science and Technology*, Vol. 126, 2022, p. 107657. https://doi.org/https://doi.org/10.1016/j.ast.2022.107657.

[18] Zhao, J., and He, C., "Physics-Based Modeling of Viscous Ground Effect for Rotorcraft Applications," *Journal of the American Helicopter Society*, Vol. 60, No. 3, 2015, pp. 1–13. https://doi.org/doi:10.4050/JAHS.60.032006.

[19] Andronikos, T., Papadakis, G., Riziotis, V. A., Prospathopoulos, J. M., and Voutsinas, S. G., "Validation of a cost effective method for the rotor-obstacle interaction," *Aerospace Science and Technology*, Vol. 113, 2021, p. 106698. https://doi.org/https://doi.org/10.1016/j.ast.2021.106698.

[20] Tan, J. F., Cai, J. G., Barakos, G. N., Wang, C., and Huang, M. Q., "Computational Study on the Aerodynamic Interference Between Tandem Rotors and Nearby Obstacles," *Journal of Aircraft*, Vol. 57, No. 3, 2020, pp. 456–468. https://doi.org/10.2514/1.C035629.

[21] Ruchała, P., and Grabowska, K., "Problems of an aerodynamic interference between helicopter rotor slipstream and an elevated heliport," *Journal of KONES*, Vol. 26, 2019, pp. 189–196. https://doi.org/10.2478/kones-2019-0072.

[22] Caprace, D.-G., Ventura Diaz, P., and Yoon, S., "Simulation of the Rotorwash Induced by a Quadrotor Urban Air Taxi in Ground Effect," *79th Vertical Flight Society Annual Forum and Technology Display*, West Palm Beach, Florida, 2023.

[23] Pulliam, T., "High Order Accurate Finite-Difference Methods: as seen in OVERFLOW," *20th AIAA Computational Fluid Dynamics Conference*, 2012. https://doi.org/10.2514/6.2011-3851.

[24] Chaderjian, N. M., and Ahmad, J., "Navier-Stokes Assessment of Test Facility Effects on Hover Performance," *American Helicopter Society 71st Annual Forum*, Virginia Beach, VA, 2015.

[25] Chaderjian, N. M., "Quantitative Approach for the Accurate CFD Simulation of Hover in Turbulent Flow," *International Conference on Computational Fluid Dynamics 11*, Maui, Hawaii, 2022, pp. 1–27.

[26] Jespersen, D., Pulliam, T., Buning, P., Jespersen, D., Pulliam, T., and Buning, P., "Recent enhancements to OVERFLOW," *35th Aerospace Sciences Meeting and Exhibit*, 1997. https://doi.org/10.2514/6.1997-644.

[27] Yoon, S., Chaderjian, N. M., Pulliam, T. H., and Holst, T. L., "Effect of Turbulence Modeling on Hovering Rotor Flows," *45th AIAA Fluid Dynamics Conference*, Dallas, 2015. https://doi.org/10.2514/6.2015-2766.

[28] Yoon, S., Lee, H. C., and Pulliam, T. H., "Computational Analysis of Multi-Rotor Flows," *54th AIAA Aerospace Sciences Meeting*, 2016. https://doi.org/10.2514/6.2016-0812.

[29] Ventura Diaz, P., and Yoon, S., "Computational Study of NASA's Quadrotor Urban Air Taxi Concept," *AIAA Scitech Forum*, 2020. https://doi.org/10.2514/6.2020-0302.

[30] Ventura Diaz, P., and Yoon, S., "High-Fidelity Simulations of a Quadrotor Vehicle for Urban Air Mobility," *AIAA Scitech Forum*, 2022. https://doi.org/10.2514/6.2022-0152.

[31] Chan, W., III, R. G., Rogers, S., and Buning, P., "Best Practices in Overset Grid Generation," *32nd AIAA Fluid Dynamics Conference*, 2002. https://doi.org/10.2514/6.2002-3191, 6th Symposium on Overset Grids and Solution Technology.

[32] Chatelain, P., and Koumoutsakos, P., "A Fourier-based elliptic solver for vortical flows with periodic and unbounded directions," *Journal of Computational Physics*, Vol. 229, No. 7, 2010, pp. 2425–2431. https://doi.org/10.1016/j.jcp.2009.12.035.

[33] Caprace, D.-G., Gillis, T., and Chatelain, P., "FLUPS: A Fourier-Based Library of Unbounded Poisson Solvers," *SIAM Journal on Scientific Computing*, Vol. 43, No. 1, 2021, pp. C31–C60. https://doi.org/10.1137/19M1303848.

[34] Jeanmart, H., and Winckelmans, G., "Investigation of eddy-viscosity models modified using discrete filters: A simplified regularized variational multiscale model and an enhanced field model," *Physics of Fluids*, Vol. 19, No. 5, 2007, p. 055110. https://doi.org/10.1063/1.2728935.

[35] Cocle, R., Bricteux, L., and Winckelmans, G., "Scale dependence and asymptotic very high Reynolds number spectral behavior of multiscale subgrid models," *Physics of Fluids*, Vol. 21, No. 8, 2009, p. 085101. https://doi.org/10.1063/1.3194302.

[36] Cocle, R., Dufresne, L., and Winckelmans, G., "Investigation of multiscale subgrid models for LES of instabilities and turbulence in wake vortex systems," *Lecture Notes in Computational Science and Engineering*, Vol. 56, 2007, pp. 141–159.

[37] Winckelmans, G. S., *Encyclopedia of Computational Mechanics*, John Wiley & Sons, Ltd, 2004, Chap. Vortex Methods, pp. 129–153. https://doi.org/10.1002/0470091355.ecm055.

[38] Chatelain, P., Curioni, A., Bergdorf, M., Rossinelli, D., Andreoni, W., and Koumoutsakos, P., "Billion vortex particle Direct Numerical Simulations of aircraft wakes," *Computer Methods in Applied Mechanics and Engineering*, Vol. 197, No. 13, 2008, pp. 1296–1304. https://doi.org/10.1016/j.cma.2007.11.016.

[39] Mimeau, C., and Mortazavi, I., "A Review of Vortex Methods and Their Applications: From Creation to Recent Advances," *Fluids*, Vol. 6, No. 2, 2021. https://doi.org/10.3390/fluids6020068.

[40] Cottet, G.-H., and Koumoutsakos, P., *Vortex Methods, Theory and Practice*, Cambridge University Press, 2000.

[41] Sbalzarini, I. F., Walther, J. H., Bergdorf, M., Hieber, S. E., Kotsalis, E. M., and Koumoutsakos, P., "PPM A highly efficient parallel particle mesh library for the simulation of continuum systems," *Journal of Computational Physics*, Vol. 215, 2006, pp. 566–588. https://doi.org/10.1016/j.jcp.2005.11.017.

[42] Caprace, D.-G., Winckelmans, G., and Chatelain, P., "An immersed lifting and dragging line model for the vortex particle-mesh method," *Theoretical and Computational Fluid Dynamics*, Vol. 34, 2020, pp. 21–48. https://doi.org/10.1007/s00162-019-00510-1.

[43] van Rees, W. M., Leonard, A., Pullin, D. I., and Koumoutsakos, P., "A comparison of vortex and pseudo-spectral methods for the simulation of periodic vortical flows at high Reynolds numbers," *Journal of Computational Physics*, Vol. 230, No. 8, 2011, pp. 2794–2805. https://doi.org/10.1016/j.jcp.2010.11.031.

[44] Chatelain, P., Backaert, S., Winckelmans, G., and Kern, S., "Large eddy simulation of wind turbine wakes," *Flow, Turbulence and Combustion*, Vol. 91, No. 3, 2013, pp. 587–605. https://doi.org/10.1007/s10494-013-9474-8.

[45] Caprace, D.-G., Chatelain, P., and Winckelmans, G., "Wakes of rotorcraft in advancing flight: A large eddy simulation study," *Physics of Fluids*, Vol. 32, No. 8, 2020, p. 087107. https://doi.org/10.1063/5.0015162.

[46] Caprace, D.-G., and Ning, A., "Large Eddy Simulation for Empirical Modeling of the Wakes of Three Urban Air Mobility Vehicles," *Journal of the American Helicopter Society*, Vol. 68, 2023, p. 042002. https://doi.org/https://doi.org/10.4050/JAHS.68.042002.

[47] Caprace, D.-G., Winckelmans, G., and Chatelain, P., "Assessment of the Vortex Particle-Mesh Method for Efficient LES of Hovering Rotors and their Wakes," *AIAA Scitech Forum*, 2021. https://doi.org/10.2514/6.2021-0738.

[48] Caprace, D.-G., Ning, A., Chatelain, P., and Winckelmans, G., "Effects of rotor-airframe interaction on the aeromechanics and wake of a quadcopter in forward flight," *Aerospace Science and Technology*, 2022, p. 107899. https://doi.org/https://doi.org/10.1016/j.ast.2022.107899.

[49] Angot, P., Bruneau, C., and Fabrie, P., "A penalization method to take into account obstacles in incompressible viscous flows," *Numerische Mathematik*, Vol. 81, 1999, pp. 497–520.

[50] Rasmussen, J. T., Cottet, G.-H., and Walther, J. H., "A multiresolution remeshed Vortex-In-Cell algorithm using patches," *Journal of Computational Physics*, Vol. 230, 2011, pp. 6742–6755. https://doi.org/10.1016/j.jcp.2011.05.006.

[51] Mimeau, C., Cottet, G.-H., and Mortazavi, I., "Direct numerical simulations of three-dimensional flows past obstacles with a vortex penalization method," *Computers & Fluids*, Vol. 136, 2016, pp. 331 – 347. https://doi.org/10.1016/j.compfluid.2016.06.020.